Seismic resilience assessment-informed UAV task allocation framework for post-earthquake survey

Zhengyang Hou [a,b], Tian You [c], Wei Wang [a,b,*]

[a] *State Key Laboratory of Disaster Reduction in Civil Engineering, Tongji University, Shanghai, 200092, China*
[b] *Shanghai Engineering Research Center for Resilient Cities and Intelligent Disaster Mitigation, Shanghai, 200092, China*
[c] *College of Civil Engineering, Nanjing Tech University, 30 South Puzhu Road, Nanjing, 211816, China*

A B S T R A C T

In recent years, unmanned aerial vehicles (UAVs) have been widely used in post-earthquake investigations due to their versatility. However, the existing task allocation of the UAVs is primarily based on the basic physical attributes of the target points, which contain limited seismic information. The seismic indicators derived from seismic resilience assessment provide a more detailed reflection of earthquake damage and have the potential to enhance the rationality and efficiency of task allocation in post-earthquake surveys. Thus, a framework to introduce the regional seismic resilience assessment into the task allocation of the survey is proposed. The framework defines the basic attributes of target points based on the regional seismic resilience assessment. The methods for constructing constraints and objective functions relevant to post-earthquake surveys are also provided. The framework consists of three parts: seismic resilience assessment, indicator conversion, and problem-solving. The proposed framework aims to provide a feasible approach for integrating real earthquake disaster scenarios with UAV task allocation, promoting the practical application of related research findings in the real world. The case studies based on the San Francisco Bay Area testbed and the 2014 South Napa California earthquake are taken as examples to introduce the framework and demonstrate the framework's effectiveness and feasibility under both actual conditions and simulated conditions. Comparisons among solutions based on different kinds of basic attributes are made to validate the feasibility of the proposed framework, and the result proves that a higher investigation efficiency can be obtained after the introduction of seismic resilience indicators into UAV task allocation.

1. Introduction

Earthquakes can cause substantial damage to urban functionality and significantly threaten the safety of residents' lives and property. Once the city is attacked by the earthquake, it is necessary to delineate the extent of the affected area and identify the disaster situation immediately [1,2]. The rapid post-earthquake investigation is essential for maximizing the effectiveness of rescue operations and for conducting a thorough evaluation and documentation of the damage scenario [3]. In recent years, unmanned aerial vehicles (UAVs) have been widely used in post-earthquake investigations due to their versatility. Compared with traditional aircraft, UAVs have the advantage of high deployment speed, infrastructure independence, and cost-effectiveness [4]. Moreover, UAVs deliver

higher-resolution images than satellites and maintain flexibility in various weather conditions [5].

However, limited by the battery capacity and maximum flying distance, efficient planning of UAVs during the investigation is hence important to collect more post-earthquake disaster information. The optimization of the UAV tasks to achieve more targets in a shorter time is a typical operational research problem known as vehicle routing problems (VRPs) in the field of automatic control [6]. This question further leads to two sub-questions: task allocation and path planning [7]. Task allocation and path planning are interconnected yet distinct concepts for UAVs. Task allocation involves the strategic distribution of tasks among a group of UAVs, ensuring that each drone is assigned tasks that align with its capabilities, thereby optimizing overall efficiency, effectiveness, or other pertinent metrics. Task allocation requires consideration of the UAVs' capabilities, the urgency and importance of the tasks, and the availability of resources, aiming to achieve fairness, efficiency, and practicality in the distribution of tasks [8]. Path planning refers to the process of determining an optimal route for a UAV to travel from a starting point to a destination within a given environment. The process accounts for obstacle avoidance, flight capability limitations (e.g. minimum turning radius, maximum turning speed), and energy conservation, among other factors [9]. Path planning focuses on how a UAV navigates safely and efficiently, ensuring successful mission completion in complex environments [10]. In a word, task allocation determines what will the UAVs do while path planning addresses how will the UAVs do it. Although these are separate issues, they are typically interrelated in practical scenarios. Effective task allocation can guide path planning, and efficient path planning can enhance the execution of tasks, improving overall mission success and safety.

In this research, UAV-based post-earthquake investigation falls within the realm of task allocation. The typical technical routes and research methods to solve the problem of UAV task allocation mainly include five methods [6]: optimization algorithm (linear programming, integer programming, mixed integer linear programming, etc.), heuristic algorithm (genetic algorithm, particle swarm optimization, ant colony algorithm, etc.), market mechanism method, game theory method, and machine learning method. No matter what method is chosen to solve the task allocation problem, the base attributes of the target points are necessary to determine the priority of different target points and are needed to calculate the objective function. For post-earthquake investigation, the target points refer to all the objects that need to be investigated. Depending on the scale of the problem, the target point can be a single building, a community, a region, a city, or even a province. Different types of target points have different basic attributes, the basic attribute of target points with bigger scales is highly correlated with that of target points with smaller scales. Through the investigation of the relevant literature, the target point of the post-earthquake investigation usually is a regional target in the field of automatic control. The common basic attributes of the investigation targets include building area [11–14], number of buildings [12], population [12,13,15–17], epicentral distance [12,16,17], number of important buildings (hospitals, schools, fire stations) [15,17,18], number of possible heavily damaged buildings [13,18]. In summary, the previous paper assigned weights to different target points through the subjective evaluation based on the basic attributes for subsequent algorithm testing, and the core of these studies is to figure out algorithms with higher efficiency or accuracy, there is little attention on the kinds of basic attributes. It should be noted that the common attributes in previous post-earthquake investigation task allocation are all basic geometric and physical information. Due to the lack of further analysis using seismic engineering methods, it is difficult to essentially reflect the characteristics of an earthquake with a certain magnitude and the loss of buildings in the region. What's more, the existing attributes fail to reflect the emphasis on severely damaged buildings and areas in post-earthquake investigations.

Recently, the concept of seismic resilience has attracted interest across multiple disciplines and has been taken as a potential method to overcome the incoordination between the seismic design principle and the challenge of urban earthquake disaster prevention [19–21]. The core idea of urban seismic resilience is the ability of the urban infrastructure and societal framework to endure earthquakes, thereby preventing immediate chaos or permanent damage [22–25]. To transform theoretical seismic resilience into practical applications, the appropriate resilience indicator system should be built to carry out specific urban seismic resilience assessments. According to FEMA P-58 [26] and other resilience- and performance-based methods, economic losses, downtime, and functional recovery times are recommended to evaluate the seismic resilience of buildings. These three indicators have been proven to be effective on different kinds of buildings even some new structural styles like self-centering structural systems [27]. In addition, the resilience-based method is not only limited to assessing a single building but also is suitable for building complexes with various structural types. Burton et al. [28,29] introduced a framework to evaluate the seismic resilience of a community enhanced by rocking spine system by linking the limit state of the single building to the post-earthquake recovery and seismic functional loss. Hulsey et al. [30] used the REDi Rating System supported by ARUP to research the relationship between the seismic functional loss of the community and the usage of safety cordons.

As a research hotspot of seismic engineering, the resilience indicators are used to describe the buildings and regions' functional loss after a real earthquake or a simulated one, which means the resilience indicators can also be regarded as a kind of basic attributes of buildings under an earthquake with a certain magnitude. Moreover, due to the convertibility between the resilience indicators of a building and a region [31], the similar basic attributes of a region can also be calculated. Therefore, it's a potential method to introduce the seismic resilience indicators into the task allocation of UAV-based rapid post-earthquake investigation. In this paper, a framework to combine the seismic resilience assessment with the UAV task allocation in the post-earthquake survey is proposed to further improve the efficiency of post-earthquake investigation. Section 2 is a brief introduction to the proposed framework. The detailed introductions of the parts are given in Section 3 to Section 5. The case studies based on the San Francisco Bay Area testbed [32] and the 2014 South Napa California earthquake are provided in Section 6 to demonstrate the framework's effectiveness and feasibility under both actual conditions and simulated conditions.

2. Framework

The framework workflow is shown in Fig. 1. There are mainly three parts: seismic resilience assessment indicator conversion, and problem-solving. The following are the specific steps in each part.

2.1. Seismic resilience assessment

This part completes the seismic resilience assessment of individual buildings in the target region, providing resilience indicators as a data foundation for subsequent calculations. This part mainly includes the following steps.

(a) Collect the basic physical information of the buildings in the target region including number of stories, structural type, location, completion date, structural area, etc. The basic information is used to build a multi-story lumped-mass shear model [33,34] for every single building.
(b) Engineering demand parameters (EDPs) of each building are calculated through incremental dynamic analysis (IDA) [35,36] and the probability distributions of EDPs including residual and maximum interstory drift ratio (IDR), peak floor acceleration (PFA) are obtained from the calculation result.
(c) Intensity measure (IM) fields of the target region are simulated through the Monte Carlo method [37,38] with the epicenter of the Hayward Earthquake [39]. Ground motion prediction equations (GMPEs) [40,41] are introduced to estimate the median IM and the deviation for each building site.
(d) Seismic resilience indicators (repair time, repair cost, and functional loss time) of each building are calculated based on the EDPs from step (b) and the IM field in step (c). Each building gains a series of seismic resilience indicators in one IM field simulation.

2.2. Indicator conversion

This part involves converting the seismic resilience indicators of the grid into the basic attributes of region target points in the task allocation. The entire study region is divided into a specified number of grids based on the requirements. The seismic resilience indicators of each grid are then calculated based on the seismic resilience indicators of the buildings within the grid. For repair time, repair cost, and functional loss time, different calculation methods are chosen to match the characteristics of the corresponding indicators [31]. All the target grids are grouped into four clusters according to different attributes by the K-means clustering algorithm. The four clusters correspond to four seismic damage states including slight, moderate, extensive, and complete. The grids in the same cluster have similar indicators and are more likely to have similar function loss after an earthquake. The seismic resilience indicators of all target points are normalized during the clustering, and the normalized seismic resilience indicators are then defined as the basic attributes of the target points for the following task allocation solving.

2.3. Problem-solving

This part abstracts the UAV task allocation for post-earthquake surveys into an operations research problem. An improved clone selection algorithm (CSA) is introduced to solve the specific task allocation with different seismic damage information collection methods. The basic attributes of the target points in the task allocation are the normalized seismic resilience indicators in Part 2. A method is proposed to define seismic damage information amount based on the residual IDR. The constraints and objective functions for post-earthquake UAV surveys are also defined. Comparisons among solutions based on different basic attributes of the grid target points are made to illustrate the relationship between survey efficiency and basic attribute selection.
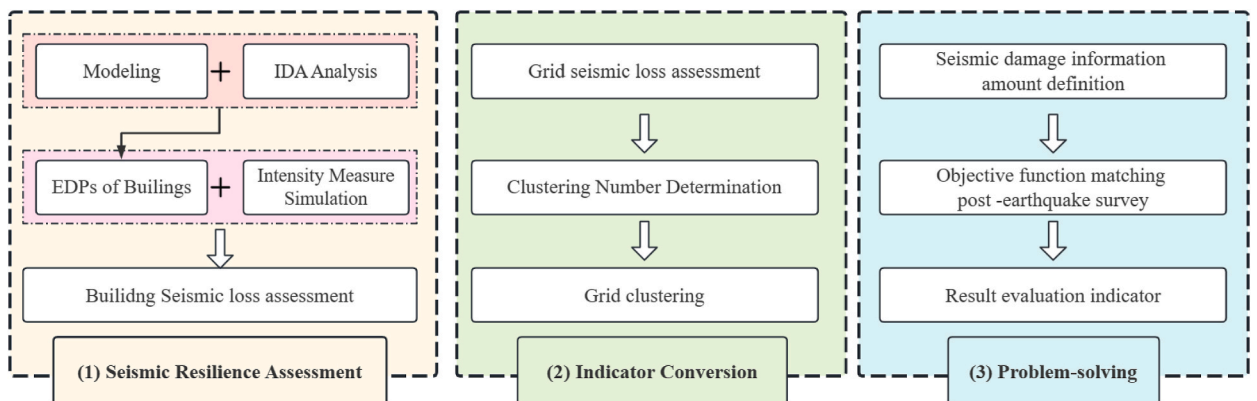

Fig. 1. Framework for task allocation of UAV-based rapid post-earthquake investigation considering seismic resilience assessment.

It should be noted that the proposed framework is flexible and can be replaced based on accessible data and survey objectives. The principle for replacement is to ensure that every step has the same form of input from the previous and output for the other steps. For example, more detailed finite element models of the buildings can be developed if more resources like structural design drawings are available in Part 1 step (a). By introducing the component information, seismic loss assessment can be finished from a component-level or building-level in Part 1 step (d) according to FEMA P-58 [26] and Hazus [42] methods respectively. Additionally, the clustering operation in Part 2 and the objective function in Part 3 are arranged for the seismic analysis principle in this paper, other related grid processing methods and objective functions can be used for other principles.

The earthquake and seismic resilience information for introducing the framework is gathered from the pre-earthquake simulation and analysis. The results based on simulated scenario earthquakes can be used to formulate contingency plans in advance before a real earthquake occurs. If information (e.g. acceleration time histories) of an earthquake can be quickly obtained from the seismic station immediately after the earthquake occurs and sufficient computing power is available, the IDA in Part 1 step (b) can be performed through the real earthquake information instead of the simulation. This calculation result can be taken as the input for Part 1 step (c) and the following steps leading to a result with more pertinence for this earthquake.

Additionally, the steps included in the framework are essentially regression, clustering, and classification tasks. In recent years, with the widespread use of machine learning and artificial intelligence in civil and earthquake engineering [43–45], the steps in the framework can be implemented using artificial intelligence agent models under certain assumptions after further analysis and refinement. This would enhance computational efficiency and better account for the effects of seismic randomness and uncertainty.

3. Regional seismic resilience assessment

Past research has made a large number of studies for the building and regional seismic resilience assessment in developing related models, tools, and workflows. This study focuses on how to integrate the regional seismic resilience assessment with UAV task allocation. The Hazus Methodologies method is introduced in this research for the assessment of the buildings, while the method in Refs. [27,31] is applied for the regional seismic resilience assessment. A brief introduction to the four steps of the assessment is provided in this section. For a more detailed description of regional seismic resilience assessment, please refer to the review reference [46].

3.1. Simplified finite element structural model

The finite element (FE) model of the buildings within the region is a necessary condition for conducting seismic resilience assessment, multi-story lumped mass shear models [33] are introduced in this paper. The building floor is simplified into a concentrated mass and structures between the adjacent floors are modeled as a shear spring to simulate the lateral resisting systems. The basic assumption of the structural model is that the floor mass m and elastic stiffness k of each floor have the same value. This assumption is introduced to simplify the calculation of k which means k can be calculated through the T_1 (fundamental period of building) and m in model analysis. No more assumptions and conditions are required. m equals mass density multiplied by total plan area and then divided by the number of stories. T_1 is derived from different structural types' T_0 (typical period) and N_0 (stories) which are provided in Hazus [42]. T_1 is calculated from Eq. (1) with the assumption N (the number of stories) is proportional to the fundamental period.

$$T_1 = \frac{N}{N_0} T_0 \tag{1}$$

A schematic diagram of the model is shown in Fig. 4 (a). The parameters of the shear spring's hysteretic response are gathered from a hysteretic rule and a capacity curve to describe the deformation histories' influence on the hysteretic response. The definition of hysteretic parameters and the capacity curve are shown in Fig. 2 (b) and 2 (c) respectively. All the parameters required for the definition can be found in the databases and tables provided by Hazus [42]. For specific calculation methods, please refer to reference [27,33].

3.2. IDA analysis

With the FE models of buildings, IDA can be implied to calculate the seismic response and the corresponding EDPs. It's a
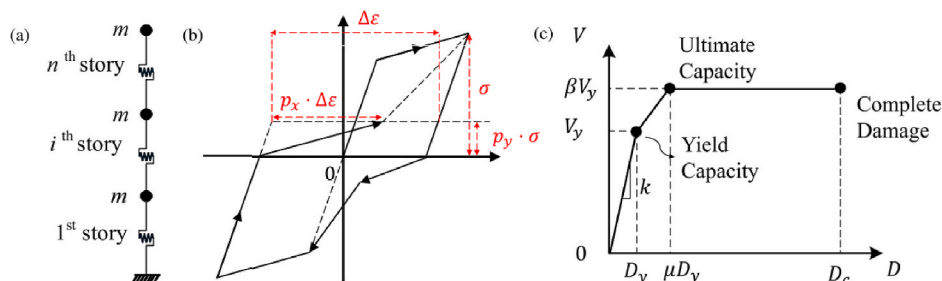

Fig. 2. (a) Multi-story lumped mass shear model (b) definition of hysteretic parameters (c) capacity curve.

computationally intensive task to perform the IDA for every structure in the study region. Therefore, a grouping simplified method is introduced to reduce the cost of the calculation. For buildings of different area intervals, only one building in the interval is arranged to perform IDA and all the other buildings share the same result. The width of the interval is 100 m^2. According to minimum numbers recommendations in FEMA P-58 [26], eight seismic intensities and ten ground motion records are prepared to carry out IDA. Ten ground motion records are selected from the twenty-two far-field records provided in FEMA P659 [47]. The seismic intensities in descending order include: 2.0, 1.5, 1.0, 0.8, 0.6, 0.4, 0.2, and 0.1 *g*. The time step is set as 0.1 s in the calculation. With the above preparation, the EDPs of each building can be calculated through IDA, and the probability distributions of EDPs (residual and maximum interstory drift ratio, peak floor acceleration) are further gathered from the calculation results.

It should be noted that the number of seismic intensities (8) and ground motion records (10) in this study is close to the minimum numbers recommended in FEMA P-58 [26] which are eight and seven. Additional combinations of parameters are required for a more reliable result and the reduction may introduce errors in IDA. The reliability of the numbers used in this study is proved through trial calculations in Ref. [27]. The result shows that the reliability of IDA analysis with intensities less than 1.0 is acceptable and more error occurs with higher intensities. Thus, the intensities are designed to be less than 1.0 *g* in the following steps as much as possible. With the above guarantee, the simplified method is thought to be acceptable for IDA.

3.3. Simulation of intensity field with specific epicenter location

The seismic load of a single building depends on the intensity of its site. For buildings in the region, the intensity of the building sites is different from each other because the distance from the sites to the epicenter and the soil conditions differ. Therefore, the IMs at the building site given a certain magnitude of scenario earthquake should be simulated to calculate the seismic response of all buildings in the region. The specific scenario earthquake is defined by its epicenter and magnitude, which can be selected according to the former earthquake record and related database. Different periods' spectral accelerations $S_a(T)$ are necessary to be calculated because different site conditions have different fundamental periods. The IM field of the study region is formed with the $S_a(T)$ of the building sites for each period. The IM of a single building site is simulated from Eq. 2

$$\ln IM = \mu_{\ln IM} + \delta W + \delta B \tag{2}$$

where μ_{lnIM} is the logarithmic mean of IM which is calculated from GMPEs [39,40]. δW and δB are random variables to represent within-event and between-event residuals respectively. The NGA-West2 GMPEs [40] are introduced in this research to estimate μ_{lnIM} and standard deviations of δW and δB. A detailed explanation of Eq. (2) and GMPEs is available in Refs. [37,38,47–50]. The above introduction is just a brief overview of IM field simulation. More detailed information can be found in Ref. [51]. To consider the randomness in the process of earthquake propagation, hundreds of simulations in the Monte-Carlo procedure are usually carried out for the IM field simulation. According to the recommendation in Ref. [27], 500 simulations were finished in this research.
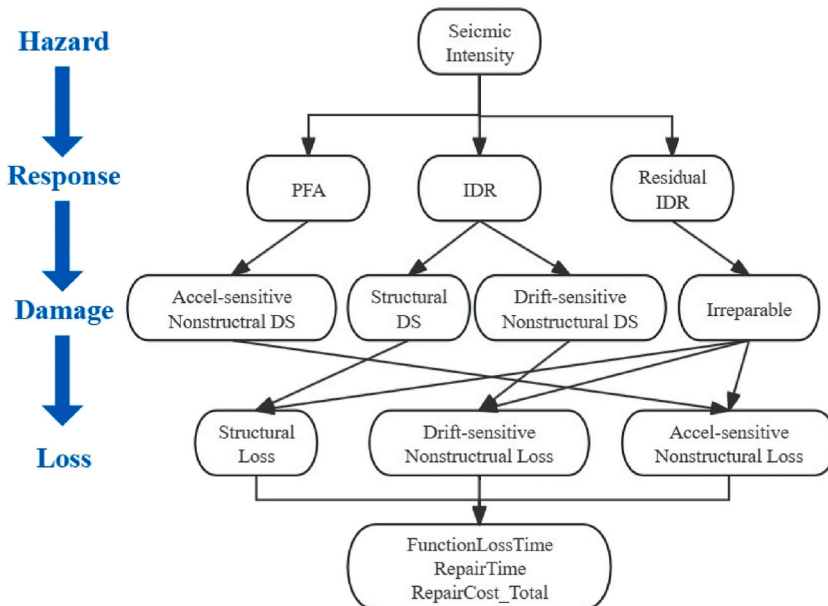

Fig. 3. Seismic resilience loss calculation process.

3.4. Seismic resilience assessment of buildings

The simulated IM field provides the intensity for each building site to assess seismic resilience loss. The calculation method for seismic resilience loss of a building is shown in Fig. 3. As mentioned in Section 3.2, IDA has provided the probabilistic distributions of EDPs for different intensities of the building site. Therefore, residual IDR, PFA, and IDR are selected as the seismic responses of a single building and the values of the responses can be sampled randomly according to the distributions of corresponding intensity. This operation assumes that EDPs follow a jointly lognormal distribution.

Afterward, seismic responses are used to confirm the damage state of the building. There are three damage types: acceleration-sensitive nonstructural damage, drift-sensitive nonstructural damage, and structural damage [42]. The maximum PFA decides acceleration-sensitive nonstructural damage while the maximum IDR decides drift-sensitive nonstructural damage and structural damage. According to the Hazus Earthquake Technical Manual [52], the damage state includes four levels: complete, extensive, moderate, and slight. The fragility curves of the four levels are also provided in Hazus [52]. The variance and median of the fragility curve depend on the seismic level and structural type. Besides, the residual IDR is used to estimate the complete damage state which means the repair cost of the building is too high to accept [26]. The threshold of residual IDR is 1 % to determine whether this irreparable situation occurs. Based on Hazus 42 [42], the calculation of resilience indicators requires the premise of the building's damage states. For example, the repair cost ratios for the calculation of repair costs corresponding to the four damage states are different. The total seismic resilience loss is the sum of three damage types' loss.

4. Conversion of resilience indicators into basic attributes of target points

The conversion of resilience indicators and the basic attributes of target points serves as a crucial link that integrates seismic resilience assessment with UAV task allocation for post-earthquake surveys. While target points of different scales have different basic attributes, the seismic resilience assessment can provide indicators that are commensurate with the scale. This section uses a regional target to demonstrate the integration of seismic indicators with basic attributes. Additionally, the method for constructing constraints and objective functions relevant to post-earthquake surveys is also outlined. Similar approaches can be applied to define the basic attributes, constraints, and objective functions for target points of other scales.

4.1. Grid seismic loss assessment

The region target here is conceptually opposed to that of a single building, rather than referring to the entire study region. The number of target points significantly impacts the complexity of the problem and the time required for the calculation. To reduce computational cost, the study region should be partitioned into grids and each grid is a target point of the study. An appropriate partitioning method can be selected based on computational conditions to balance between detail and efficiency. Several examples were given in the subsequent case studies.

The seismic resilience indicators of a building include average intensity, repair time, repair cost, and functional loss time, and the basic attributes of a grid are also supposed to contain these four indicators. The average intensity of a grid is the mean value of the average intensity of the buildings in the grid. The repair cost of a grid can be derived directly from the sum of the repair cost of the buildings within the grid. In addition to the mean value, other confidence level values or probability density functions of the building resilience indicators can also be used as representative values for the grid's resilience indicator. The use of these methods reflects the decision-maker's emphasis on the current earthquake scenario, thus enabling more flexible achievement of different decision-making objectives. For the other two time-related seismic indicators, it should be noted the repair processes among different buildings may exhibit dependencies [28,31,53]. For example, the repair of one building relies on the restoration of functionality in a nearby power station and the repair of different infrastructure systems is also interdependent. This dependency relationship is complex because there may be mutual or circular dependencies involved. The research on this topic falls outside the scope of this paper and the related research can be found in Ref. [53]. Therefore, an intuitive approach is introduced to estimate the repair time and functional loss time of a grid. The repair time of a grid is determined by the longest repair time among the buildings within the grid, and similarly, the functional loss time of a grid equals the longest functional loss time of the buildings in that grid. Expect the seismic resilience indicators, there are also three basic attributes of a grid including location, total building area, and number of buildings. The location of a
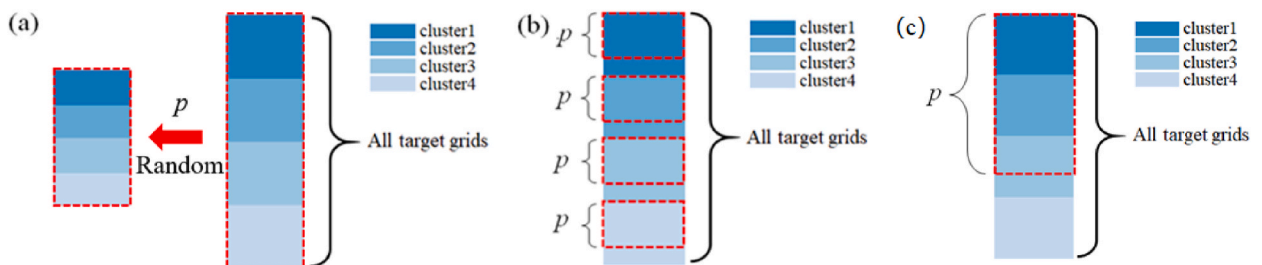

Fig. 4. Examples of representative grids selection methods.

grid is determined by the coordinates of its center point. The total building area is equal to the sum of the areas of all buildings within the grid. With these attributes, all attributes of a grid target point are available.

4.2. Grid clustering

After a scenario earthquake, grids with similar attributes tend to display similar damage levels [54]. Therefore. it is feasible to investigate only a part of the grids to representatively reflect the damage condition of grids sharing a similar damage level to rapidly ascertain the overall extent of earthquake damage [15,55]. The grid target points in the study region can be divided into several clusters by serval clustering criteria with different attributes. There are six clustering criteria as shown in Table 1 and each criterion includes one basic attribute of the grid. The seismic resilience indicators of all target points should be normalized during the clustering, and the normalized seismic resilience indicators are then defined as the basic attributes of the target points for the following task allocation. It should be noted that the clustering criteria can encompass multiple parameters theoretically. But sorting of the grids also needs to be accomplished except clustering. Clustering criteria with multiple parameters can group the grids into different clusters, but the grids within one cluster can't be ranked with a clear physical meaning.

C-N and C-A are the basic physical attributes that frequently appear in past research. C-RC, C-RT, and C-L are seismic resilience indicators of a grid while C-IM is the attribute related to the generating process of seismic resilience indicators. These resilience indicators reflect the idea of introducing the seismic resilience assessment into the task allocation of UAV-based rapid post-earthquake surveys. In the subsequent case studies, six solutions are obtained respectively based on these six criteria. The difference among these six solutions can demonstrate the advantages of adopting seismic resilience indicators.

The K-means algorithm is introduced in this study to cluster the grids. The K-means algorithm is a popular clustering technique used to partition data into multiple groups. The number of clusters is determined by the elbow method [56] which is a common method used to determine the optimal value of k in the K-means algorithm. The elbow method involves plotting the within-cluster sum of squares (WCSS) or sum of the squared errors (SSE) against a range of k values. The key step is to identify the elbow point on the plot, where the rate of decrease in WCSS or SSE sharply changes. The k of the elbow point is considered the best value for the clustering task.

4.3. Representative grids selection

After clustering the grids, several grids from each cluster need to be selected as representatives. The ratio of the representative grid number to the total number of grids is marked as coverage ratio p. The method for selecting representative grids is actually related to the objectives of the decision-maker's information collection process. For example, three different selection methods are shown in Fig. 4. The first method shown in Fig. 4 (a) means the representative grids in each cluster are randomly selected with a ratio of p. This method is applicable for situations where a comprehensive understanding of the seismic damage within each cluster is required, thereby guiding rescue operations. The second method shown in Fig. 4 (b) means selecting representative grids from different clusters respectively. Grids that are more likely to experience severe damage in every cluster are selected adhering to the proportion of p. This method is used to investigate the extent of damage within each cluster in a relatively relaxed time, thereby acquiring more comprehensive information about seismic damage. The method shown in Fig. 4 (c) means grids that are more likely to experience severe earthquake damage are selected as the representative grids with a ratio of p. This method is applicable for swiftly identifying regions with the most severe seismic damage within a limited time.

5. Task allocation for UAV-based rapid post-earthquake survey

The previous sections have introduced the basic attributes of the target points and the data foundation necessary for solving the task allocation. Solving the task allocation has been proven to be an NP-hard [57], where the time and difficulty of finding the optional solution increase very rapidly with the increase of target points' number. In past research, many methods have been proposed to solve task allocation of UAVs. The Clonal Selection Algorithm (CSA) is an optimization algorithm inspired by the biological immune system, specifically modeling the processes of antibody recognition, cloning, mutation, and selection to solve various optimization problems [58–60]. The CSA is a typical optimization method for task allocation aiming to maximize the amount of information collected or minimize the time cost. An improved clonal selection algorithm (CSA) is proposed in this paper to solve the task allocation for UAV-based rapid post-earthquake surveys. The flowchart of the improved CSA is shown in Fig. 5. It should be emphasized that the main idea of this study is to integrate seismic resilience assessment with post-earthquake UAV task allocation. Therefore, the improvement of CSA is aimed at enhancing adaptability to decision-making objectives, rather than optimizing computational efficiency in task allocation. Part 1 and Part 2 have completed data preparation and defined the basic attributes of the target points based on the seismic resilience indicators. This part abstracts the UAV task allocation for post-earthquake surveys into an operations research problem and provides a feasible method to ensure the completeness of the proposed framework. It should be noted that other methods

Table 1
Attributes used for clustering.

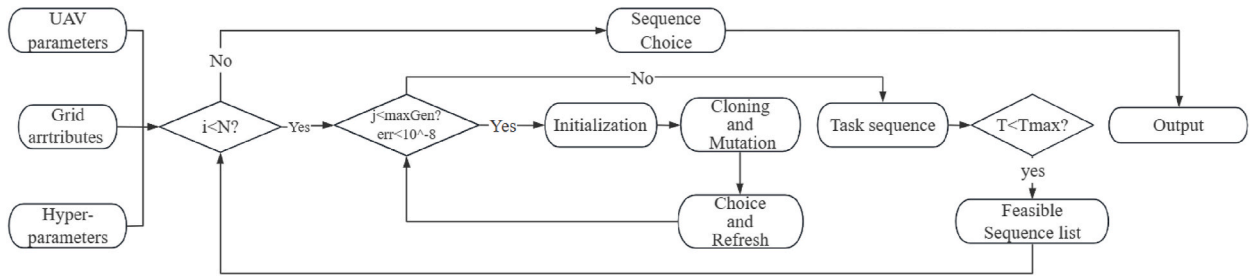| Clustering criterion	C-N	C-A	C-RC	C-RT	C-L	C-IM
Attributes	Number of buildings	Total building area	Repair cost	Repair time	Function loss time	Average intensity

Fig. 5. The flowchart of the improved CSA.

that meet the decision-making requirements and computational demands can also be used to solve the problem.

5.1. Basic framework of the improved CSA

The algorithm involves a combination of random initialization, cloning, mutation, affinity evaluation, and both inner and outer loop processes to achieve an efficient solution. The steps are outlined as follows.

(a) Initialization

Several potential solutions for the task allocation problem are generated randomly as initial antibodies. Each solution represents a specific task sequence for each UAV, indicating the order in which UAVs will visit each grid. The affinity function is used to evaluate the quality of each solution. It reflects how well a solution satisfies the task allocation criteria which is set as the corresponding value of the objective function. A total of N antibodies (solutions) are randomly initialized, forming the initial population for the algorithm.

(b) Cloning and Mutation

Each antibody is cloned n times. Cloning involves creating multiple copies of a given solution, which serves as the basis for further optimization. For each cloned antibody, a mutation is applied. This mutation involves exchanging two segments of the task sequence which is introduced detail in the following Section 5.2. This step allows the algorithm to explore different solution possibilities and prevent the search from converging too early.

(c) Selection and Refresh

After cloning and mutation, the affinity function values of the n cloned antibodies are calculated. These clones are then compared to the original antibody (the parent) to determine which one performs best. Only the antibody with the highest affinity value among the $n+1$ solutions (original + clones) is retained, while the others are discarded. The top 50 % of antibodies (with the highest affinity function values) are retained for the next generation. The remaining population is replenished with $N/2$ new randomly generated antibodies to maintain population diversity and ensure continuous exploration of the solution space. After the population update, the affinity values of the entire population are recalculated and sorted. The antibody with the highest affinity is selected as the best solution for the current iteration.

(d) Inner Loop Termination:

The inner loop focuses on refining the solutions through multiple iterations of cloning, mutation, and selection. This loop continues until the maximum number of iterations is reached or the difference between the optimal value of two consecutive iterations falls below a predefined threshold, indicating convergence.

(e) Outer Loop Process:

After completing an inner loop, the output (best solution) is checked against a predefined time threshold. This threshold represents the maximum time allowed for the UAV task allocation to complete. If the output satisfies the time constraint, it is added to the feasible sequence list, indicating that this solution is acceptable. Otherwise, the next iteration of the inner loop is initiated without adding the current solution to the list.

(f) Outer Loop Termination:

The outer loop continues to run until the maximum number of iterations is reached. The goal of the outer loop is to find multiple feasible solutions, which are then stored in the feasible sequence list. Once the outer loop terminates, the solutions in the feasible

sequence list are evaluated based on their overall performance.

(g) Output. The output of the algorithm includes the task sequence for each UAV in the investigation, the time of the investigation, and the value of an indicator to evaluate the result.

Compared with the traditional CSA, an external loop has been integrated to get several feasible solutions that come from the inner time optimization loop. Based on these superior feasible solutions, the most appropriate one for the application scenario is selected based on various evaluation metrics. With this improvement, the versatility and scalability of the proposed framework can be enhanced for different scenarios.

5.2. Encoding of antibody and mutation rules

Each antibody corresponds to a feasible solution. For task allocation, particular emphasis is placed on the sequence of grid points traversed by all the UAVs. Considering that the labels of grid target points are a series of discrete values, a discrete encoding strategy from the realm of real-number encoding is introduced to conduct the encoding of antibodies. For multi-UAV task allocation, the sequence of each UAV is obtained by truncating the whole sequence according to a specific pattern. The sequences of different UAVs are expected to have the same or similar lengths to ensure a balanced distribution of tasks and this operation is arranged to primarily consider the load-balancing principle in UAV performance metrics [6]. For example, assuming 12 grid target points whose indexes are sequentially numbered from 1 to 12 need to be visited by three UAVs. The codes of one possible whole sequence and the corresponding sequences of three UAVs are shown in Fig. 6 with the assumption that each UAV departs from and returns to its respective base. The mutation of antibodies is performed by exchanging two indexes of the sequence such as the exchange of index 4 and index 7 in Fig. 6.

5.3. Objective function

The objective function of the algorithm is determined based on the targets of surveys. During the post-earthquake survey, more seismic damage information is expected to be collected in a short period for a comprehensive understanding of the regional damage situation. Therefore, investigation time and amount of seismic damage information are the fundamental considerations for constructing the objective function. In this study, the investigation time is used to construct the objective function while the quantity of seismic damage information is used to develop an evaluation indicator for the results.

The investigation time refers to the longest task time among all the UAVs participating in the investigation. Clearly, this time cannot exceed the maximum flight time of the UAV without considering recharging during flight. The task time includes the time allocated for flight between different target points and the time dedicated to investigating grids. Therefore, the time-related objective function can be expressed as Eq. (3).

$$T = \max \left(\min \sum t_{fi} + t_{wj} \right)_k \quad i,j \leq N_k, k \leq K \tag{3}$$

where t_{fi} is the time allocated on the ith flight and N_k is the sequence length of the kth UAV. K is the number of UAVs participating in the survey. For a sequence with N_k target points, because it needs to depart from and return to its respective base, there are a total of N_k
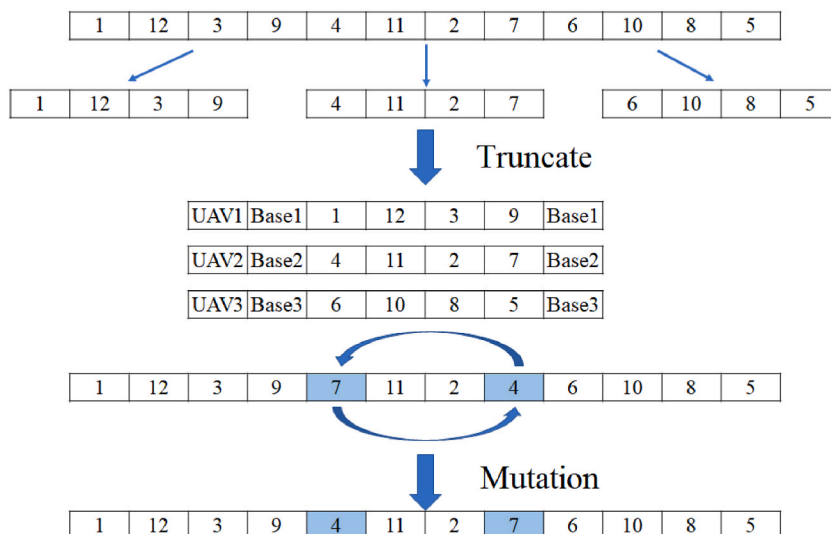

Fig. 6. A schematic illustration of the encoding method and mutation.

flight processes which means that the maximum value of i is N_k. t_{fi} is calculated by dividing the distance between adjacent grids by the speed of the kth UAV. t_{wj} is the work time in the jth grid which is related to the performance of the UAV, the number of buildings in the grid, and the survey time for each building. t_{wj} equals the survey time of buildings added with the flight time within the grid. Therefore, accurately estimating t_{wj} is challenging because determining the actual flight route in every grid and the survey time of every building is difficult. To simplify the calculation, t_{wj} of the jth grid is calculated from Eq. (4).

$$t_{wj} = \frac{1}{v_k} \times \left(\sqrt{n_j} \times L_x + L_y \right) \times \frac{\sqrt{n_j} - 1}{\sqrt{n_j} + 1} \tag{4}$$

where n_j is the number of buildings in the jth grid. L_x and L_y are the lengths of the grid in the east-west and north-south directions, respectively. v_k is the flight speed of kth UAV. Eq. (4) assumes that the buildings are uniformly distributed within the grid and the UAVs can successfully survey all the buildings following the order shown in Fig. 7. This assumption is based on the method of coverage path planning which aims to plan a route for covering all the interest points in a certain area [54,61]. Even if buildings are not distributed as assumed, a similar route can still be identified to investigate all buildings according to the route planning method in Fig. 7. Eq. (4) is generalized from the cases in which n_j is a square number and then promoted to all integers. For grids with only one building or no buildings, the flight time within the grid is set as zero. Like the seismic resilience indicators, t_{wj} can also be taken as one of the grid's attributes.

5.4. Result evaluation indicator

The amount of seismic damage information is used to develop an evaluation indicator. The indicator should be able to measure the efficiency of the UAV's sequence in which more seismic damage information is expected to be collected in a shorter time. The amount of seismic information present within a grid needs to be defined. In this study, a method based on the probability of irreparability as shown in Fig. 8 is used to measure the amount of information within a grid. S_i is used to represent the seismic information amount of ith building. As mentioned in Section 3, once the residual IDR of a building is larger than 1 %, the building is considered to be irreparable which demonstrates that the building has suffered severe damage and even collapsed. More seismic information can be collected and analyzed from the severely damaged buildings. During the 500 times IM field simulations, the ith building will have a probability of irreparability in each simulation, the expectation of these 500 probabilities P_i can be used to measure whether the building is irreparable. It should be noted that the probability that both the ith building and the jth building are irreparable can't be calculated by adding p_i and p_j up directly because their irreparable probabilities may affect each other.

Usually, the information amount of an object should be a scalar that can be directly added, rather than a probabilistic value. Therefore, the P_i of the buildings are standardized to 0-1 marked as $\overline{P_i}$ to reflect the irreparable degree's rank of the ith building among all buildings. In addition, the relationship between $\overline{P_i}$ and the information amount of a building S_i is not linear. For example, a building with $\overline{P_i} = 0.2$ and a building with $\overline{P_i} = 0.1$ may both in a slight damage state which means the information of these two buildings doesn't differ significantly. However, the information amount of a building with $\overline{P_i} = 0.8$ exceeds twice the sum of two buildings with $\overline{P_i} = 0.4$, because these two buildings are in not severe damage states with less seismic information and their information is partly duplicated while the building with $\overline{P_i} = 0.8$ is in extensive or even complete states. It can be summarized that the increase ratio of S_i is faster than the increase ratio of $\overline{P_i}$ for buildings with bigger $\overline{P_i}$ but slower for buildings with smaller $\overline{P_i}$. It's difficult to build an accurate mapping function between $\overline{P_i}$ and S_i. For simplification, the value of S_i is assumed as the square of the value of $\overline{P_i}$ ($S_i = \overline{P_i}^2$) in this study. This assumption leads a higher increase speed of S_i for all $\overline{P_i}$ and can match the phenomenon in bigger $\overline{P_i}$ interval. Although the relative increase speed in smaller $\overline{P_i}$ interval doesn't match the phenomenon, the values of S_i in smaller $\overline{P_i}$ interval are small and don't differ significantly which can match the corresponding similarity of S_i. Then, the informational content of the grid can be expressed as the sum of the S_i of all buildings within the grid. Variable S_n is introduced to represent the information amount of the nth grid in the sequence. With the above preparation, the evaluation indicator F of the solution sequence gathered from the improved CSA can be expressed by Eq. (5), Eq. (6), and Eq. (7).

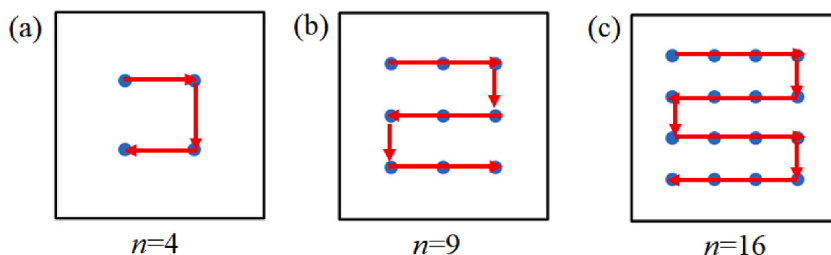$$S_n = \sum_1^j S_j \quad n = 1, 2, 3, \cdots, n_j \tag{5}$$

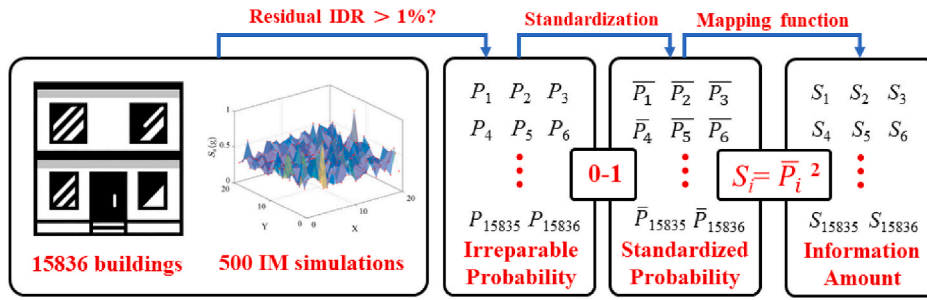**Fig. 7.** Schematic of simplified flight time calculation within the grid.

Fig. 8. The assessment of the information amount.

$$S = \sum_{1}^{n} S_n \quad n = 1, 2, 3, \cdots, N \tag{6}$$

$$F = \frac{S}{T} \tag{7}$$

where N is the length of the whole sequence and n_j is the number of buildings in the jth grid. the physical meaning of F is the rate of information collection per unit time of the sequence, with a higher value indicating a greater efficiency of the sequence. In the feasible solution list of the inner loop, the one with the largest F is selected as the final output.

6. Case study

After introducing the entire framework, two specific case studies are arranged to demonstrate how to apply the proposed framework. The two cases are the San Francisco Bay Area Testbed case based on the simulation and the 2014 South Napa California Earthquake case based on the real seismic damage survey. When applied to these two different types of cases, the specific implementation of the framework varies slightly. As mentioned in Section 2, the steps within the framework can be adjusted according to the specific conditions.

6.1. Case study on the San Francisco Bay area testbed

The research area of this case study is part of the San Francisco Bay Area testbed which contains 15836 buildings with detailed information from the SimCenter and all the data can be found on the official website [32]. The basic information about the buildings includes plan area, structural type, location, building stories, footprint, year of construction, and occupy class. The testbed is suitable for applying the Hazus Methodologies to calculate the seismic resilience loss because occupancy class and structural type are compliant
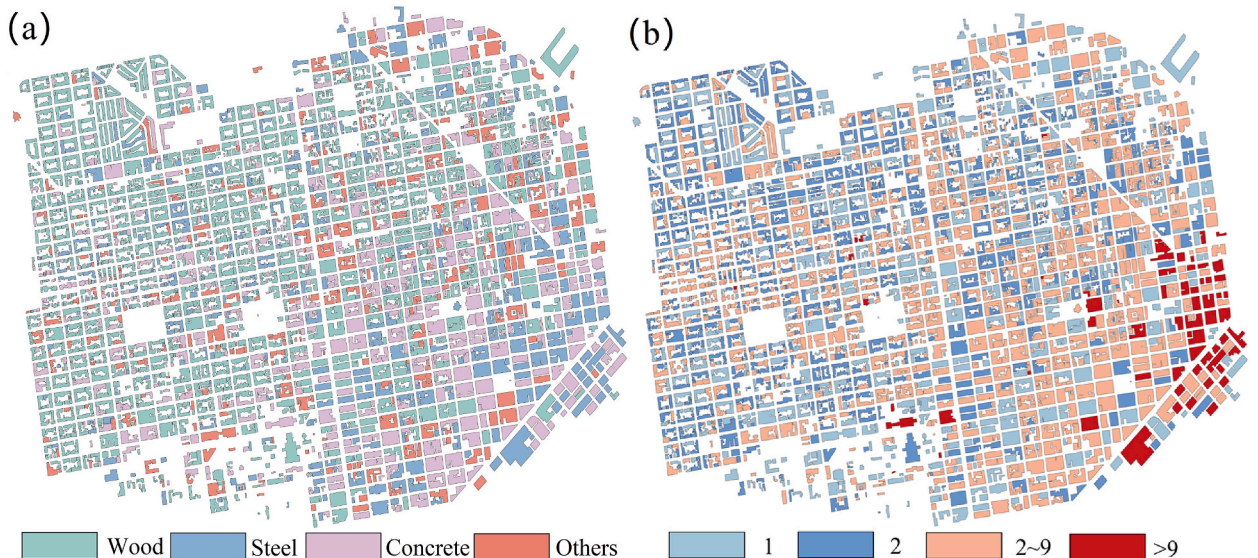

Fig. 9. (a) Structural types and (b) building stories.

with categories provided in the related Hazus Inventory [52]. Fig. 9 shows the structural types and the building stories of the study area and Fig. 10 shows the frequency distributions of serval basic information. The majority of the building stories are fewer than 10 stories and most buildings were built later than 1900. The W1 is the largest number of structural types and is mainly concentrated in the northwest of the study area. Table 2 shows the structural types and corresponding labels of the buildings within the research region. Different structural types mean the different replacement cost of buildings which is provided through cost per sq. feet in the Hazus Inventory [52]. The multi-story lumped mass shear models of all 15836 buildings are built for the following steps.

According to the simplified IDA analysis method introduced in Section 3.2, 6137 buildings are selected as the representatives of 15836 buildings in this study which means only 38.8 % of the original calculation time is needed after the simplification. The EDPs of each building are calculated through IDA, and the probability distributions of EDPs (residual and maximum interstory drift ratio, peak floor acceleration) are further gathered from the statistical results.

The scenario earthquake in this study is selected according to the Hayward earthquake by setting the same epicenter and magnitude ($M_W = 7$). The reason for this selection is that the San Francisco Bay Area testbed applied in this research is in the seismic influence area of the Hayward earthquake as shown in Fig. 11 and this scenario earthquake has also been used as a case example in previous research [27,39].

With the information of the buildings and the scenario earthquake, the IM field of the study area is simulated through the method introduced in Section 3.3. 500 simulations are carried out and the magnitude is set as seven. A simulation result of the IM field is shown in Fig. 12. Fig. 12 (b) shows the spectral acceleration simulation result along the red arrow in Fig. 12 (a). The green line is the median value from GMPEs while the orange chain line considers δB. The purple curve is the simulated ln*IM* result. As mentioned in Section 3.2, the intensities are expected to be less than 1.0 g for fewer errors and most of the results are indeed less than 1.0 g.

The seismic resilience assessment of buildings is processed based on the results of IDA and IM simulation. Since there are 500 simulations of IM fields, one building after each simulation has a group of seismic responses and also a group of seismic resilience indicators (repair time, repair cost, and functional loss time). With these calculation results, the distributions of seismic resilience indicators of each building can be summarized, and the expectations of the seismic resilience indicators can also be calculated as basic attributes of the building. The average intensity of 500 simulations for sites of buildings is also taken as one basic attribute of the building.

Then, the entire region is divided into several grids, which are defined as target points for task allocation. There are three different quantity partitioning methods used in this case study including 10 × 10, 15 × 15, and 20 × 20 to demonstrate that the proposed framework is valid for multiple target numbers. Fig. 13 shows the specific grid partitioning and numbering methods of an example with 3000 buildings where each blue point is a single building. The basic attributes of each grid (location, number of buildings, total building area, average intensity, repair time, repair cost, functional loss time, work time (t_{wj}), and information amount (S_n)) are calculated based on the basic attributes of the buildings within the grid, as introduced in Section 4 and Section 5.

After partitioning the grids and calculating the basic attributes of the grid target points, all grids are clustered using K-means clustering based on the six clustering criteria in Section 4.2. The grids within the same cluster can be considered similar, and as previously mentioned, it is feasible to investigate only a subset of the grids to representatively reflect the damage condition of similar grids. Fig. 14 shows elbow plots to select k based on the C-L (function loss time) of the grids in the testbed and it can be seen that the elbow points appear in both elbow plots when $k = 4$. Apart from $k = 5$ for C-RT, $k = 4$ is the optional value for the others. For consistency, $k = 4$ is assigned to all the clustering. Additionally, the physical meanings of these four clusters can be considered as representing the various states of damage within the cluster after a scenario earthquake referring to the four damage states of a single building in Hazus. The clustering result is shown in Fig. 15 and N is the number of grids in one column or row. After the comparison between the clustering result and the seismic response of the buildings, the levels of damage are found to decrease sequentially from cluster 1 to cluster 4. The four clusters correspond to four seismic damage states including complete, extensive, moderate, and slight. The darker the color of the grids, the greater the seismic damage state is. The result of these results can be further explained with the comparison of Fig. 9 (b) which displays the distribution of the number of floors in buildings across the testbed. The majority of buildings in the testbed have fewer than ten stories. It can be seen that the buildings in the grids that are more likely to be assigned to the first cluster tend to have a larger number of stories. Within a certain range of heights, taller buildings are expected to exhibit greater responses after a scenario earthquake from the perspective of conceptual analysis. The consistency of the results between Figs. 15 and 9 (b) contributes to the reliability of the clustering method.

The method for selecting the representative grids in Fig. 4 (c) is applied in this case study which means the grids that are more likely to experience severe earthquake damage are selected as the representative grids with a ratio of p and the coverage ratio p is set as 0.75.
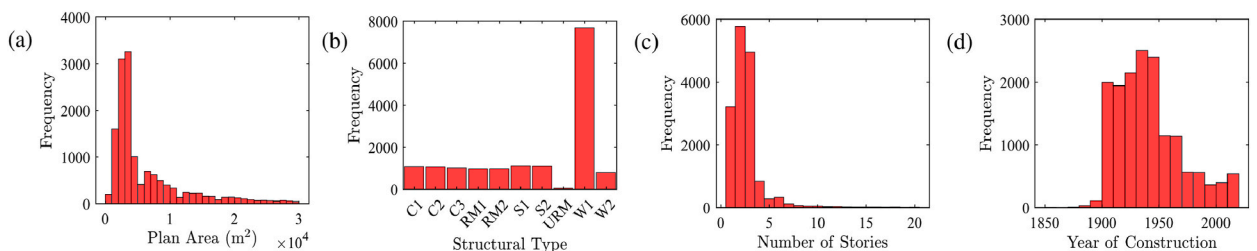

Fig. 10. Frequency distributions of (a) plan area, (b) structural type, (c) number of stories, and (d) year of construction.

Table 2
Structural types [52].

Label	Description	Label	Description
C1	Concrete Moment Frame	C2	Concrete Shear Walls
C3	Concrete Frame with Unreinforced Masonry Infill Walls	S1	Steel Moment Frame
S2	Steel Braced Frame	W1	Wood, Light Frame
W2	Wood, Commercial, and Industrial	RM	Reinforced Masonry Walls

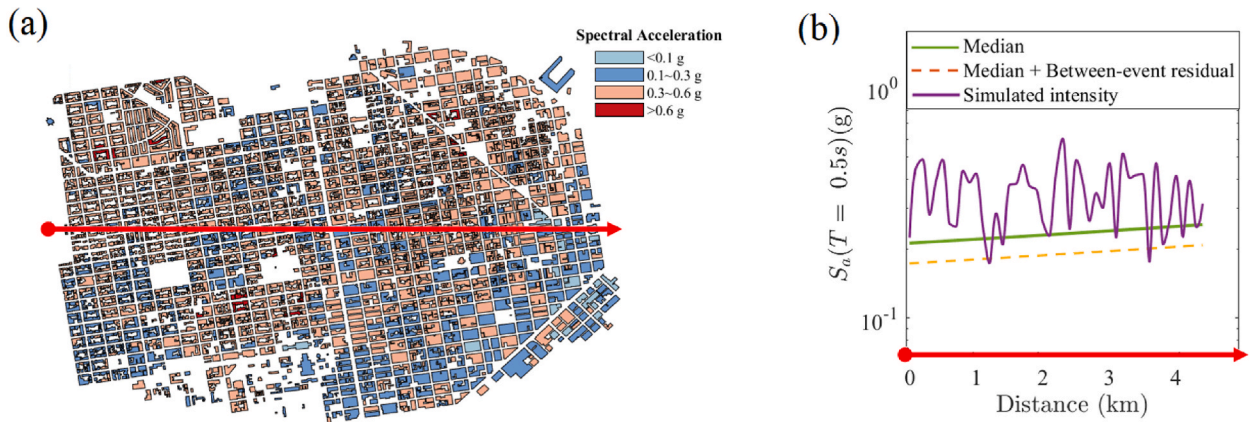**Fig. 11.** The spatial relationship between the testbed and the epicenter of the Hayward earthquake.

Fig. 12. (a) IM field from one simulation (b) Spectral acceleration simulation along the red arrow.
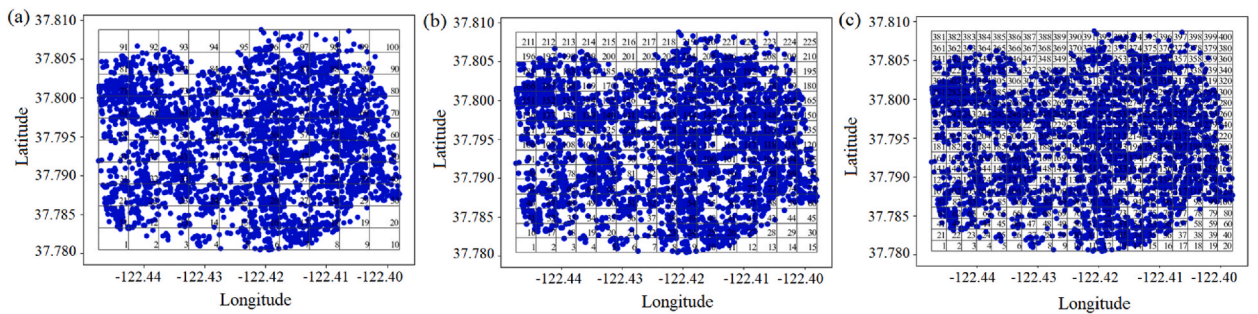
Fig. 13. Grid partitioning result of 3000 buildings (a) 10 × 10 (b) 15 × 15 (c) 20 × 20.

With the above preparation, the solution of the UAV task allocation for the post-earthquake survey can be solved through the improved CSA introduced in Section 5. The flight speed of a UAV is set as 15 m/s according to a real UAV [62]. All the UAVs are assumed to depart from and return to the same base located in the southwest of the testbed which is marked as a red circle at the bottom left corner in Fig. 16. Fig. 16 shows a solution with 10 × 10 grids based on C-RT and three different UAVs' sequence represented by different
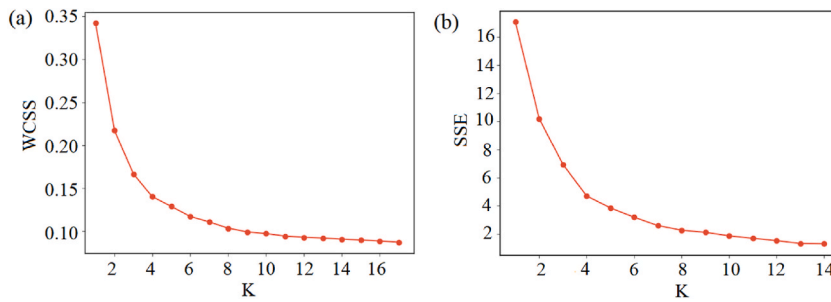
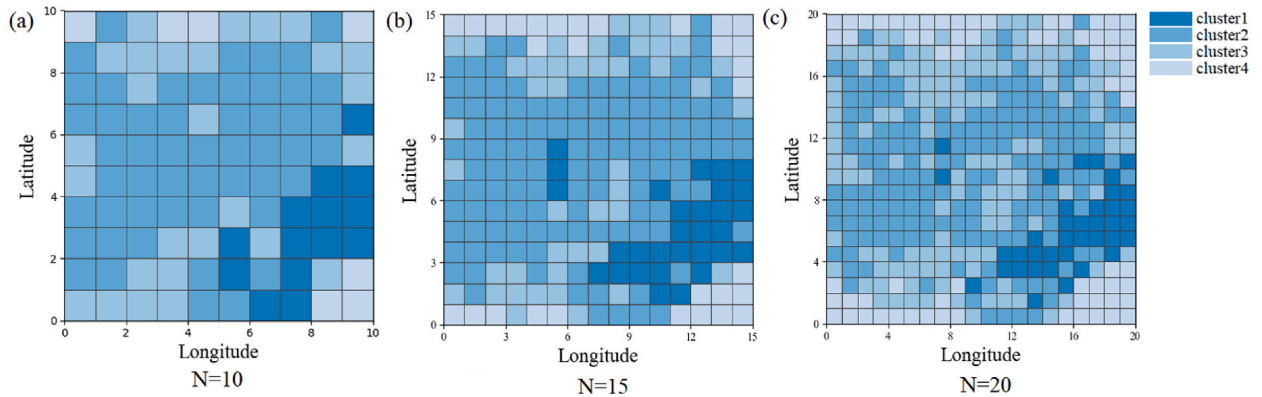**Fig. 14.** Elbow point to determine k (a) judged by WCSS (b) judged by SSE.

Fig. 15. The clustering result with different grid numbers according to C-L.
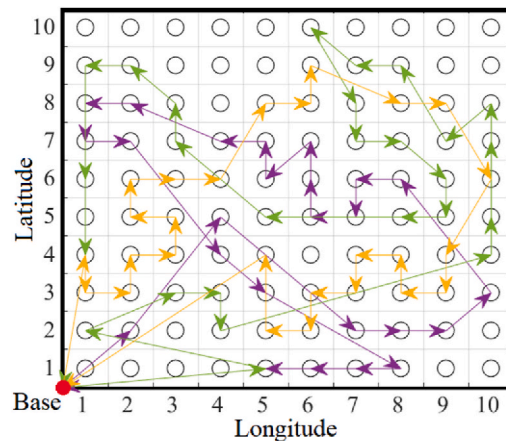

Fig. 16. Solution of three UAVs for 10×10 grids.

colors. The optional flight time from the algorithm is 9964.723 s and the F of this solution is 0.0251.

The comparison between the solutions gathered from different basic attributes is made to prove the effectiveness of introducing seismic resilience into UAV-based post-earthquake investigation. Firstly, the information amounts S of the solutions are shown in Fig. 17. On one hand, it can be seen that the results based on basic physical criterion C-N always obtain a substantial even maximum information amount S. The reason is that the sequence based on the C-N investigates the grids with the greatest number of buildings and S is directly proportional and sensitive to the number of buildings. On the other hand, the result based on C-IM (IM) always has the minimum value of S. The explanation is that the IM only reflects the information of the building sites without the seismic features provided by the structures while S is highly related to the structures' response (residual IDR). The minimum S leads to the worst result of C-IM.

Fig. 18 shows the F of solutions with different numbers of UAVs (K) and grids based on six clustering criteria. Every point in the
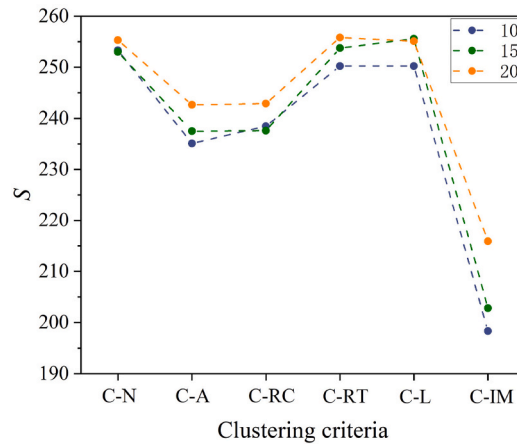
Fig. 17. Information amounts *S* of different clustering criteria.
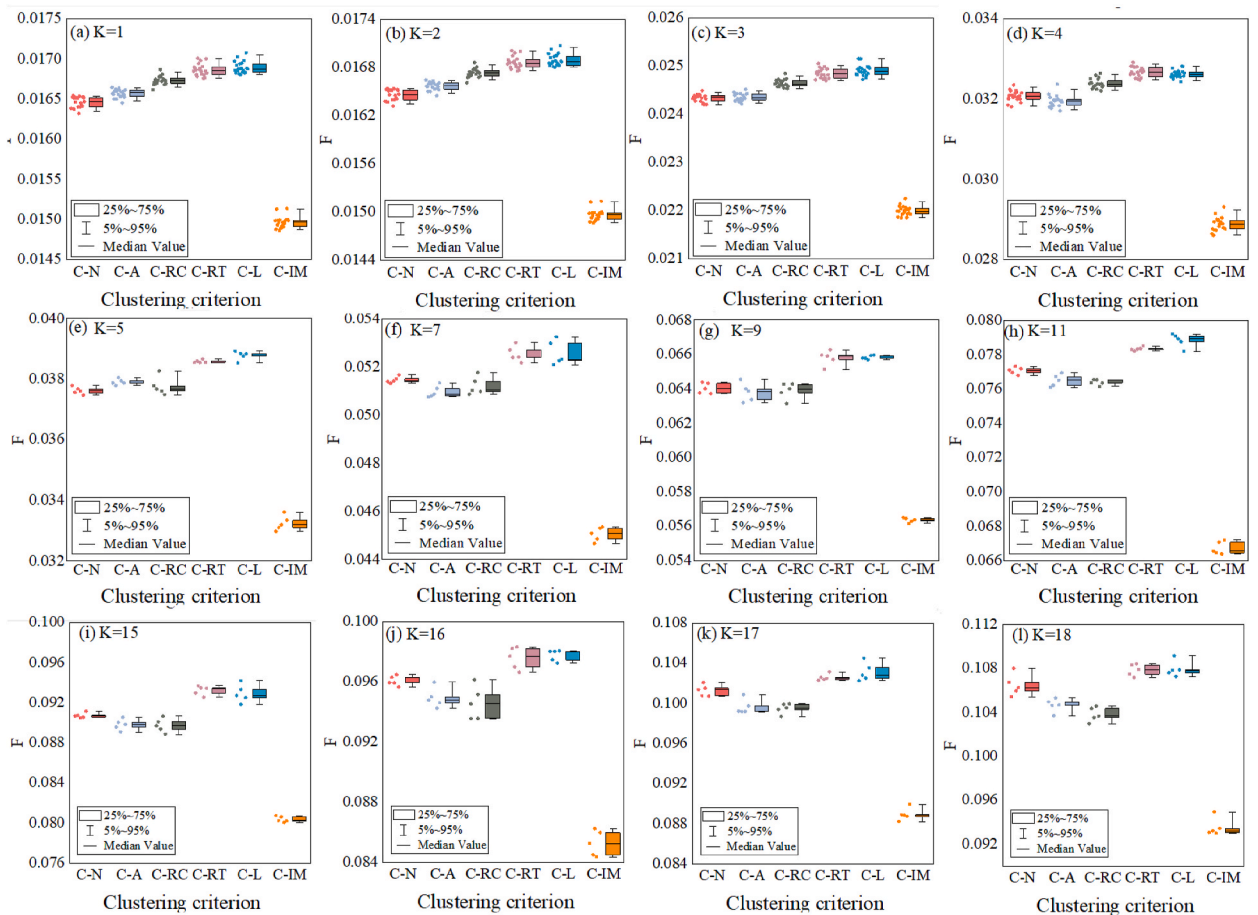

Fig. 18. Evaluation indicator F of different solutions. Subgraphs (a)–(d) are the solutions from 10*10 grids while (e)–(h) from 15*15 grids and (i)–(l) from 20*20 grids.

figure represents one solution. Subgraphs (a)-(d) are the solutions from 10*10 grids, while subgraphs (e)-(h) from 15*15 grids and subgraphs (i)-(l) from 20*20 grids. Each set of inputs is calculated multiple times to ensure the stability of the algorithm and the corresponding box shows the distribution of these solutions by indicating the median value, as well as the 5th, 25th, 75th, and 95th percentiles. Every set of inputs with 10×10 grids is calculated 20 times while 5 times for 15×15 and 20×20 due to the time cost.

From Fig. 21, it can be summarized that results based on resilience-related criteria C-RT and C-L have a higher F than those of basic physical criteria C-N and C-A while C-IM shows the worst performance. The results of C-RT and C-L come from the seismic resilience assessments, derived from further calculations using the methods in seismic engineering and structural engineering on the basic physical information of the study area. The result of the resilience assessment reflects the characteristics of the building's seismic response and better meets the needs of post-earthquake investigations. Therefore, grids ranking in the top 75 % (p) in based on resilience-related criteria contain more seismic information amount, and solution sequences that include these grids can obtain a larger F indicating a higher investigation efficiency. Moreover, the results based on basic physical criterion C-N are likely to be superior to those based on C-A and even sometimes better than C-RC. So, solutions based on C-N can be taken as feasible solutions in UAV-based post-earthquake investigation when seismic resilience assessment is challenging due to the lack of information or insufficient computational power.

6.2. Case study on the 2014 South Napa California Earthquake

To further validate the reliability and feasibility of the proposed framework, the south Napa California earthquake was selected as another case study. This particular case and scenario earthquake was chosen because Morolake Omoya et al. [63] built an open-source database including the information that is relevant to building damage and recovery assessments after the Napa earthquake. This database includes earthquake information, site investigation reports, post-earthquake building damage records, repair time of damaged buildings, and some sociodemographic information. As this database is derived from a real-world earthquake event instead of the simulated earthquakes in the San Francisco Bay area testbed case, this case study is arranged to demonstrate the framework's effectiveness and feasibility under actual conditions.

Fig. 19 shows the epicenter of the earthquake and the spatial distribution of the ATC-20 tags for buildings in Napa County. It can be included that the most significant damage is localized in the downtown region, as indicated by the concentration of red tags. There are 5.4 % of buildings assigned red tags, 47.8 % of buildings with yellow tags, and 46.8 % of buildings with green tags. The red circular in the lower right corner is the assumed UAV base in this case study. The reason for selecting this location is that the terrain here is relatively flat and open, which facilitates UAVs takeoff and operations. In practice, the choice of a UAV base location should consider a comprehensive assessment of the site conditions and the specific capabilities of the UAV. Fig. 20 shows the spatial distribution of the building's repair time which is chosen as the seismic resilience indicator in this study. It should be noted that not all buildings depicted in Fig. 19 have corresponding repair time information due to the lack of data. Therefore, it is assumed that buildings without repair time data were not damaged in the earthquake and don't need to be repaired. Sa0.3s (spectral acceleration at 0.3 s) of the building sites provided in Napa County is chosen as the IM in this case study.

As mentioned in Section 2, the proposed framework is flexible and can be exchanged by similar operations as long as every step has the same form of input from the previous and output for the other steps. The Napa base can provide sufficient data on seismic resilience assessment results, allowing the proposed framework to be implemented directly from the Part 2. Fig. 21 shows the grid partitioning result of Napa County while Fig. 22 shows the clustering result of grids based on C-RT from the method in Section 4. It can be seen that the spatial distribution of building damage observed in Figs. 19 and 22 is consistent, indicating the reliability of the employed clustering method.

With the clustering result, task allocation of the UAV-based post-earthquake investigation in Napa County can be solved by the improved CSA algorithm proposed in Section 5. For Napa data, the information collection method in Fig. 17 (a) is taken and the coverage ratio p is set as 0.75. The flight speed of a UAV is also set to 15 m/s. The location of the UAV base is the red circle in the lower right corner of Fig. 19. Fig. 23 shows the solution with 10×10 grids based on C-RT and four different UAV sequences are represented by different colors. The optional flight time from the algorithm is 10182.56 s and the F of this solution is 0.07149.

Similar to the case of the San Francisco Bay Area testbed, Fig. 24 employs the same form as Fig. 21 to show the F of solutions with different numbers of UAVs (K) and grids based on four clustering criteria for Napa data. Fig. 24(a)–(d) are the solutions from 10*10 grids, while Fig. 24(e)–(h) from 15*15 grids and Fig. 24(i)–(l) from 20*20 grids. Each set of inputs is also calculated multiple times to ensure the stability of the algorithm. From Fig. 24, it can be summarized that results based on seismic resilience-related criteria C-RT have a higher F than the solutions based on the C-N, C-A, and C-IM indicating that task allocation based on repair time can achieve the solution with the highest efficiency by collecting more seismic information in a shorter sequence time.

The conclusion gathered from Napa data is consistent with the conclusions drawn from the San Francisco Bay Area testbed demonstrating the framework's effectiveness and feasibility under actual conditions. This consistency indicates that the proposed framework is not limited to theoretical earthquake simulations within controlled testbeds but is also applicable to real-world earthquakes. In practical applications, it is not necessary to start from the first part due to the flexibility of the proposed framework (Napa case starts from Part 2). The starting step can be selected based on the available earthquake information, building data, and resilience assessment information. The steps can also be exchanged by similar operations as long as every step has the same form of input from the previous and output for the other steps as mentioned in Section 2.

7. Conclusions

This paper proposes a novel framework with the introduction of the seismic resilience assessment into the task allocation of the UAV-based post-earthquake surveys to improve survey efficiency. The core idea of the framework is to convert the seismic resilience indicators including repair time, repair cost, and function loss time as the basic attributes of the grid target points in task allocation. The framework can be applied to target points of different scales, as seismic resilience assessment can be used on multiple levels. The
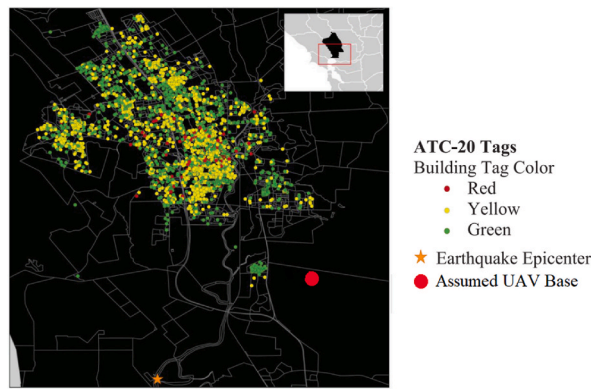
Fig. 19. The epicenter of the earthquake and the spatial distribution of the ATC-20 tags after the 2014 earthquake in Napa County [63].
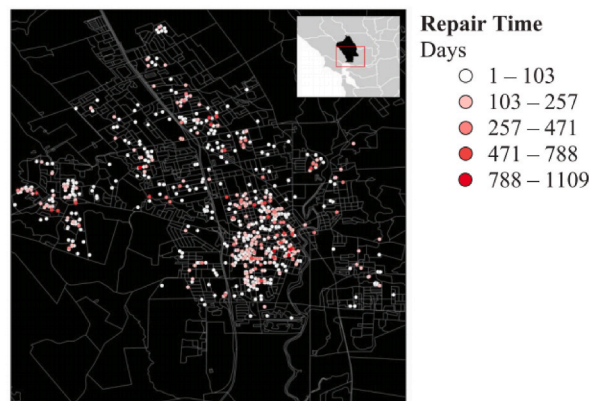

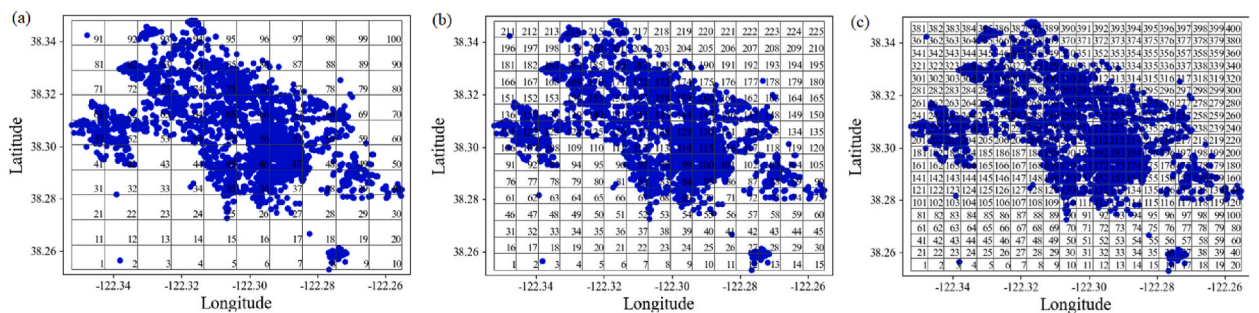**Fig. 20.** The spatial distribution of the building's repair time [63]

Fig. 21. Grid partitioning result of Napa buildings (a) 10 × 10 (b) 15 × 15 (c) 20 × 20.

target region is first divided into several grids to reduce the complexity. The indicators of the grids are calculated from the seismic resilience assessment of buildings within the grids based on the IM field simulation and IDA. The grids are further grouped into four clusters by K-means according to the basic attributes of the grids. An improved clone selection algorithm that can satisfy various investigation needs is employed to obtain feasible solutions. The case studies based on the San Francisco Bay Area testbed and the 2014 South Napa California earthquake are taken as examples to introduce the framework and demonstrate the framework's effectiveness and feasibility under both actual conditions and simulated conditions. Comparisons among solutions based on different kinds of basic attributes are made to validate the feasibility of the proposed framework, and the result proves that a higher investigation efficiency can be obtained after the introduction of seismic resilience indicators into UAV task allocation.

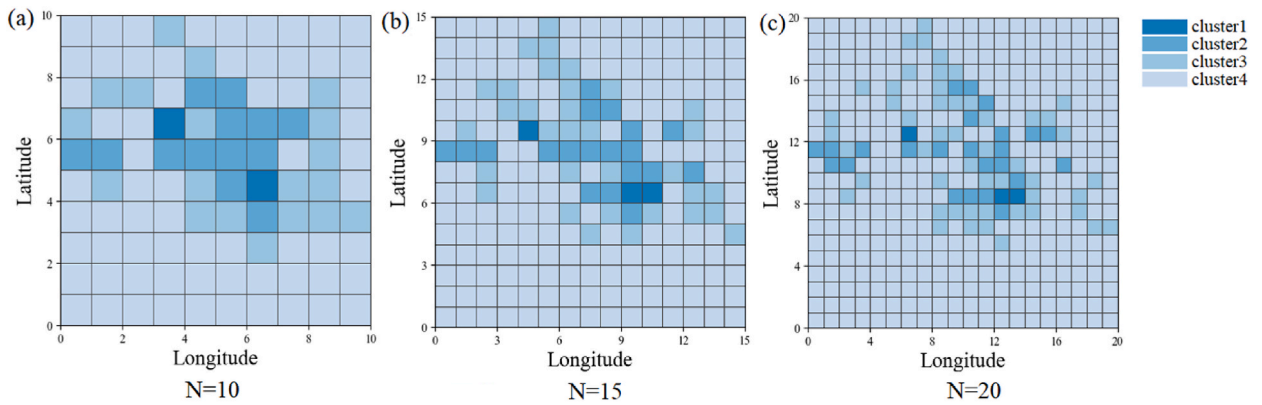From these two case studies the following conclusions can be gathered.

Fig. 22. The clustering result with different grid numbers according to C-RT.
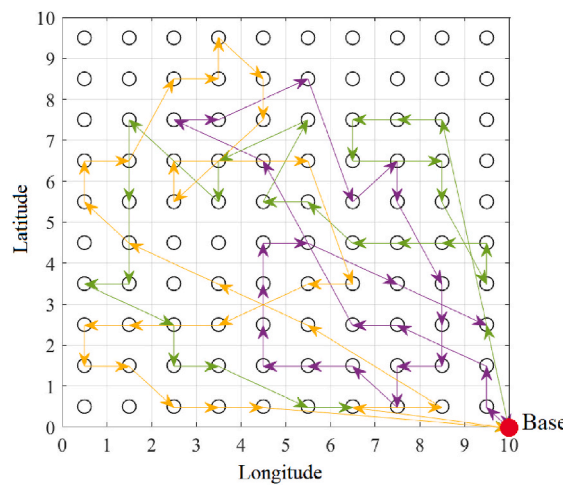

Fig. 23. Solution of three UAVs of Napa data with 10 × 10 grids.

(a) The task allocation based on the number of buildings can obtain a substantial even maximum value of S indicating that more seismic information can be collected. The reason is that the definition of seismic information amount present within a grid is positively correlated and sensitive to the number of buildings.

(b) The task allocation based on the IM shows the smallest S due to the lack of structures' response after the scenario earthquake.

(c) Task allocation based on repair time or functional loss time can achieve the solution with the highest efficiency by collecting more seismic information in a shorter sequence time. This demonstrates that introducing seismic resilience assessment into task allocation for UAV-based post-earthquake investigation can indeed lead to improvements.

(d) Once seismic resilience assessment is unavailable due to the lack of data and computational power, the feasible solution from the number of buildings can be taken as the alternative to the optimal solution.

(e) Although the framework is proposed based on simulated earthquakes, the Napa case demonstrates that task allocation solutions based on seismic resilience indicators can indeed achieve higher efficiency in real earthquake scenarios, and the proposed framework is also applicable in actual earthquake situations.

The framework is mainly grounded in the directive function of seismic resilience assessment on decision-making in earthquake-related research. The flexibility and conditional replaceability of the steps within the framework allow it to adapt actual equipment and data conditions. There are still some limitations in this study. On one hand, the same modeling method is applied for various building types and detailed structural information is unavailable, these may result in deviations in the simulated responses for certain structures. On the other hand, the quantitative method of seismic information only focuses on the information reflected by a single building while the information implied in the spatial distribution of different structures is neglected. Despite some assumptions and limitations, it is hoped that the proposed framework can offer a promising approach for related interdisciplinary research, facilitating the transformation from theory to practice.
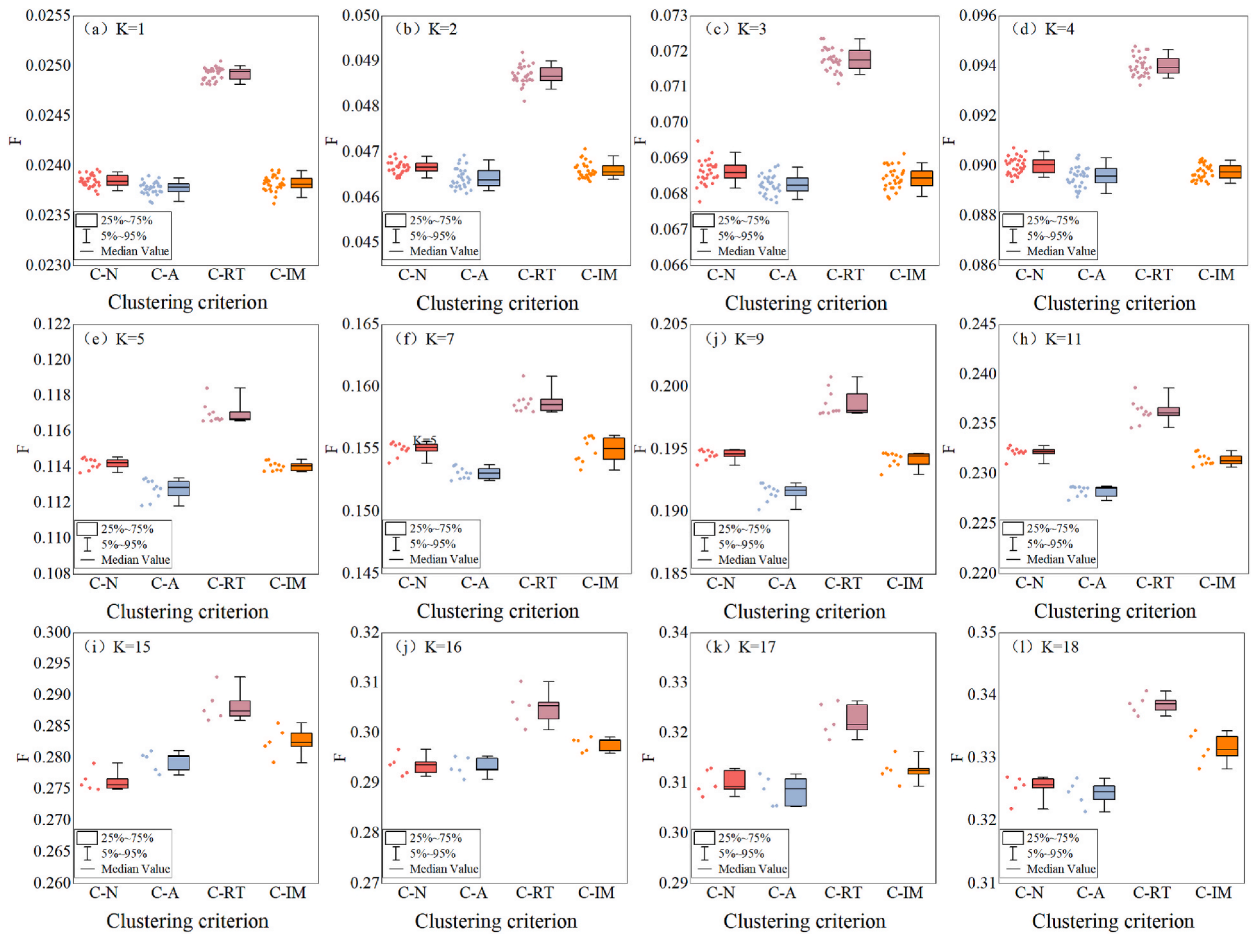
Fig. 24. Evaluation indicator F of different solutions for Napa County. Subgraphs (a)–(d) are the solutions from 10*10 grids,(e)–(h) from 15*15 grids, and (i)–(l) from 20*20 grids.

CRediT authorship contribution statement

Zhengyang Hou: Writing – original draft, Software, Methodology, Data curation, Conceptualization. **Tian You:** Writing – review & editing, Validation, Resources, Methodology, Data curation, Conceptualization. **Wei Wang:** Writing – review & editing, Validation, Supervision, Software, Funding acquisition, Formal analysis, Conceptualization.

Declaration of competing interest

The authors declare that they have no known competing financial interests or personal relationships that could have appeared to influence the work reported in this paper.

Acknowledgement

Data availability

Data will be made available on request.

References

[1] J.O. Arumala, Impact of large-scale disasters on the built environment, Leader. Manag. Eng. 12 (3) (2012) 147–150.

[2] AW Coburn, RJ Spence, A Pomonis. Factors determining human casualty levels in earthquakes: mortality prediction in building collapse, Balkema, Rotterdam, 1992, pp. 5989–5994.

[3] J.T. Qi, D.L. Song, H. Shang, N.F. Wang, C.S. Hua, C. Wu, X. Qi, J.D. Han, Search and rescue rotary-wing UAV and its application to the lushan ms 7.0 earthquake, J. Field Robot. 33 (3) (2016) 290–321, https://doi.org/10.1002/rob.21615.

[4] Adams., S., C. Friedland, M. Levitan 2010. Unmanned Aerial Vehicle Data Acquisition for Damage Assessment in Hurricane Events. 8th International Workshop on Remote Sensing for Disaster Management. Tokyo, Japan:7.

[5] D. Dominici, M. Alicandro, V. Massimi, UAV photogrammetry in the post-earthquake scenario: case studies in L'Aquila, Geomat Nat Haz Risk 8 (1) (2017) 87–103, https://doi.org/10.1080/19475705.2016.1176605.

[6] H.U. Jiawei, Zequn Jia, Sun Yantao, L. Qiang, Survey of analysis and solutions for multi UAV cooperative mission planning problem under multi-constraint conditions, Computer Science 50 (7) (2023).

[7] Z. Zhao, J. Yang, Y.F. Niu, Y. Zhang, L.C. Shen, A hierarchical cooperative mission planning mechanism for multiple unmanned aerial vehicles, Electronics-Switz 8 (4) (2019).

[8] G.M. Skaltsis, H.S. Shin, A. Tsourdos, A review of task allocation methods for UAVs, J. Intell. Rob. Syst. 109 (4) (2023), https://doi.org/10.1007/s10846-023-02011-0.

[9] Y.Y. Y., Research on Multi-UCAV Collaborative Mission Planning Method, National University of Defense Technology, Changsha, 2005.

[10] C. Goerzen, Z. Kong, B. Mettler, A survey of motion planning algorithms from the perspective of autonomous UAV guidance, J. Intell. Rob. Syst. 57 (1–4) (2010) 65–100, https://doi.org/10.1007/s10846-009-9383-1.

[11] A. Nedjati, G. Izbirak, B. Vizvari, J. Arkat, Complete coverage path planning for a multi-UAV response system in post-earthquake assessment, Robotics 5 (4) (2016) 26, https://doi.org/10.3390/robotics5040026.

[12] N. Hooshangi, A.A. Alesheikh, Developing an agent-based simulation system for post-earthquake operations in uncertainty conditions: a proposed method for collaboration among agents, ISPRS Int. J. Geo-Inf. 7 (1) (2018) 27, https://doi.org/10.3390/ijgi7010027.

[13] G.Q. Li, X.G. Zhou, J. Yin, Q.Y. Xiao, An uav scheduling and planning method for post-disaster survey, Int. Arch. Photogrammetry 40–2 (2014) 169–172, https://doi.org/10.5194/isprsarchives-XL-2-169-2014.

[14] C. Rottondi, F. Malandrino, A. Bianco, C.F. Chiasserini, I. Stavrakakis, Scheduling of emergency tasks for multiservice UAVs in post-disaster scenarios, Comput. Network. 184 (2021) 107644, https://doi.org/10.1016/j.comnet.2020.107644.

[15] B. Adsanver, E. Coban, B. Balcik, Drone routing for post-disaster damage, Assessment (2021) 1–29, https://doi.org/10.1007/978-3-030-64973-9_1.

[16] M.N. Zhu, X.H. Zhang, H. Luo, G.Q. Wang, B.B. Zhang, Optimization dubins path of multiple UAVs for post-earthquake rapid-assessment, Appl Sci-Basel 10 (4) (2020), https://doi.org/10.3390/app10041388.

[17] M.N. Zhu, X.X. Du, X.H. Zhang, H. Luo, G.Q. Wang, Multi-UAV rapid-assessment task-assignment problem in a post-earthquake scenario, IEEE Access 7 (2019) 74542–74557, https://doi.org/10.1109/Access.2019.2920736.

[18] N. Aydin, O. Yilmaz, M. Deveci, Z.H. Lv, Heuristics based optimization for multidepot drone location and routing problem to detect post-earthquake damages, Ieee T Intell Transp (2022), https://doi.org/10.1109/Tits.2022.3190698.

[19] C.H. Zhai, Y.G. Zhao, W.P. Wen, H. Qin, L.L. Xie, A novel urban seismic resilience assessment method considering the weighting of post-earthquake loss and recovery time, Int. J. Disaster Risk Reduc. 84 (2023), https://doi.org/10.1016/j.ijdrr.2022.103453.

[20] X.C. Li, Y.F. Liu, W.Y. Zhang, Y.Q. Wang, Research on an evaluation model of urban seismic resilience based on system dynamics: a case study of chengdu, China, Sustainability-Basel 15 (13) (2023), https://doi.org/10.3390/su151310112.

[21] X. Lu, H. Guan, Comparison of seismic design and performance of tall buildings based on Chinese and US design codes, in: X. Lu, H. Guan (Eds.), Earthquake Disaster Simulation of Civil Infrastructures: from Tall Buildings to Urban Areas, Springer Singapore, Singapore, 2017, pp. 225–256, https://doi.org/10.1007/978-981-10-3087-1_7.

[22] C. Liu, M. Ouyang, Z.J. Mao, X.L. Xu, A multi-perspective framework for seismic retrofit optimization of urban infrastructure systems, Earthquake, Eng Struc 51 (11) (2022) 2771–2790, https://doi.org/10.1002/eqe.3701.

[23] Y. Dong, D.M. Frangopol, Performance-based seismic assessment of conventional and base-isolated steel buildings including environmental impact and resilience, Earthquake Eng Struc 45 (5) (2016) 739–756, https://doi.org/10.1002/eqe.2682.

[24] G.P. Cimellaro, D. Solari, M. Bruneau, Physical infrastructure interdependency and regional resilience index after the 2011 Tohoku Earthquake in Japan, Earthquake, Eng Struc 43 (12) (2014) 1763–1784, https://doi.org/10.1002/eqe.2422.

[25] I. Kilanitis, A. Sextos, Integrated seismic risk and resilience assessment of roadway networks in earthquake prone areas, B Earthq Eng 17 (1) (2019) 181–210, https://doi.org/10.1007/s10518-018-0457-y.

[26] D.C.F.E.M.A. Council AT, Washington, Seismic performance assessment of buildings volume 1 - Methodology (2018). 2-1to 2-9.

[27] T. You, W. Wang, S. Tesfamariam, Effects of self-centering structural systems on regional seismic resilience, Eng. Struct. 274 (2023), https://doi.org/10.1016/j.engstruct.2022.115125.

[28] H.V. Burton, G. Deierlein, D. Lallemant, T. Lin, Framework for incorporating probabilistic building performance in the assessment of community seismic resilience, J. Struct. Eng. 142 (8) (2016), https://doi.org/10.1061/(Asce)St.1943-541x.0001321.

[29] H.V. Burton, G. Deierlein, D. Lallemant, Y. Singh, Measuring the impact of enhanced building performance on the seismic resilience of a residential community, Earthq. Spectra 33 (4) (2017) 1347–1367, https://doi.org/10.1193/040916eqs057m.

[30] A.M. Hulsey, J.W. Baker, G.G. Deierlein, High-resolution post-earthquake recovery simulation: impact of safety cordons, Earthq. Spectra 38 (3) (2022) 2061–2087, https://doi.org/10.1177/87552930221075364.

[31] T. You, W. Wang, Y.Y. Chen, A framework to link community long-term resilience goals to seismic performance of individual buildings using network-based recovery modeling method, Soil Dyn Earthq Eng 147 (2021), https://doi.org/10.1016/j.soildyn.2021.106788.

[32] F.M. Wael Elhaddad, Mats Rynge, John B. Lowe, Charles Wang, Adam Zsarnoczay, NHERI-SimCenter/WorkflowRegionalEarthquake: rWHALE (v1.1.0), Zenodo, 2019.

[33] X.Z. Lu, B. Han, M. Hori, C. Xiong, Z. Xu, A coarse-grained parallel approach for seismic damage simulations of urban areas based on refined models and GPU/CPU cooperative computing, Adv Eng Softw 70 (2014) 90–103, https://doi.org/10.1016/j.advengsoft.2014.01.010.

[34] C. Xiong, X.Z. Lu, X.C. Lin, Z. Xu, L.P. Ye, Parameter determination and damage assessment for THA-based regional seismic damage prediction of multi-story buildings, J. Earthq. Eng. 21 (3) (2017) 461–485, https://doi.org/10.1080/13632469.2016.1160009.

[35] D. Vamvatsikos, C.A. Cornell, Incremental dynamic analysis, Earthquake Eng Struc 31 (3) (2002) 491–514, https://doi.org/10.1002/eqe.141.

[36] F. Jalayer, C.A. Cornell, Alternative non-linear demand estimation methods for probability-based seismic assessments, Earthquake Eng Struc 38 (8) (2009) 951–972, https://doi.org/10.1002/eqe.876.

[37] C. Loth, J.W. Baker, A spatial cross-correlation model of spectral accelerations at multiple periods, Earthquake, Eng Struc 42 (3) (2013) 397–417, https://doi.org/10.1002/eqe.2212.

[38] K. Goda, H.P. Hong, Spatial correlation of peak ground motions and response spectra, B Seismol Soc Am 98 (1) (2008) 354–365, https://doi.org/10.1785/0120070078.

[39] A.J. Rodgers, N. Anders Petersson, A. Pitarka, D.B. McCallen, B. Sjogreen, N. Abrahamson, Broadband (0–5 Hz) fully deterministic 3D ground-motion simulations of a magnitude 7.0 hayward fault earthquake: comparison with empirical ground-motion models and 3D path and site effects from source normalized intensities, Seismol. Res. Lett. 90 (3) (2019) 1268–1284, https://doi.org/10.1785/0220180261.

[40] K.W. Campbell, Y. Bozorgnia, NGA-West2 ground motion model for the average horizontal components of PGA, PGV, and 5% damped linear acceleration response spectra, Earthq. Spectra 30 (3) (2014) 1087–1115, https://doi.org/10.1193/062913eqs175m.

[41] H. Dávalos, E. Miranda, A ground motion prediction model for average spectral acceleration, J. Earthq. Eng. 25 (2) (2021) 319–342, https://doi.org/10.1080/13632469.2018.1518278.

[42] D.C.F.E.M.A. Washington, Hazus 42. Hazus earthquake model technical manual. http://refhub.elsevier.com/S0141-0296(22)01201-9/sb51, 2020.

[43] J.J. Du, W. Wang, Surrogate model-aided global sensitivity analysis framework for seismic consequences estimation in buildings, Earthq Eng Struct D 53 (7) (2024) 2283–2312, https://doi.org/10.1002/eqe.4116.

[44] Y. Xie, M. Ebad Sichani, J.E. Padgett, R. DesRoches, The promise of implementing machine learning in earthquake engineering: a state-of-the-art review, Earthq. Spectra 36 (4) (2020) 1769–1801, https://doi.org/10.1177/8755293020919419.

[45] Y. Xie, Deep Learning in Earthquake Engineering: A Comprehensive Review (2024) 09021. ArXiv abs/2405.

[46] A. Du, X.W. Wang, Y.Z. Xie, Y. Dong, Regional seismic risk and resilience assessment: methodological development, applicability, and future research needs-An earthquake engineering perspective, Reliab Eng Syst Safe 233 (2023), https://doi.org/10.1016/j.ress.2023.109104.

[47] D.C.F.E.M.A. Applied Technology Council, Washington, Quantification of building seismic performance factors (FEMA P695) (2009) 6–15. http://refhub.elsevier.com/S0141-0296(22)01201-9/sb51.

[48] S. Esposito, I. Iervolino, Spatial correlation of spectral acceleration in European data, B Seismol Soc Am 102 (6) (2012) 2781–2788, https://doi.org/10.1785/0120120068.

[49] M. Markhvida, L. Ceferino, J.W. Baker, Modeling spatially correlated spectral accelerations at multiple periods using principal component analysis and geostatistics, Earthquake Eng Struc 47 (5) (2018) 1107–1123, https://doi.org/10.1002/eqe.3007.

[50] N. Jayaram, J.W. Baker, Correlation model for spatially distributed ground-motion intensities, Earthquake Eng Struc 38 (15) (2009) 1687–1708, https://doi.org/10.1002/eqe.922.

[51] T. You, W. Wang, Y.Y. Chen, S. Tesfamariam, Gaussian random field based correlation model of building seismic performance for regional loss assessment, Soil Dyn Earthq Eng 162 (2022), https://doi.org/10.1016/j.soildyn.2022.107501.

[52] Washington, D.C. Federal Emergency Management Agency, Hazus inventory technical manual. http://refhub.elsevier.com/S0141-0296(22)01201-9/sb51, 2021.

[53] T. You, W. Wang, Y.Y. Chen, An asynchronous simulation algorithm for post-earthquake functional recovery of interdependent infrastructure systems, Earthquake Eng Struc 53 (2) (2024) 529–544, https://doi.org/10.1002/eqe.4028.

[54] K. Yagci Sokat, I.S. Dolinskaya, K. Smilowitz, R. Bank, Incomplete information imputation in limited data environments with application to disaster response, Eur. J. Oper. Res. 269 (2) (2018) 466–485, https://doi.org/10.1016/j.ejor.2018.02.016.

[55] B. Adsanver, E. Çoban, B. Balcik, A predictive multistage postdisaster damage assessment framework for drone routing, Int. Trans. Oper. Res. 32 (2) (2024) 626–668. https://onlinelibrary.wiley.com/doi/full/10.1111/itor.13429.

[56] R. Tibshirani, G. Walther, T. Hastie, Estimating the number of clusters in a data set via the gap statistic, J. Roy. Stat. Soc. B 63 (2001) 411–423.

[57] X. Zhang, X. Chen, UAV task allocation based on clone selection algorithm, Wireless Commun. Mobile Comput. 2021 (2021) 5518927, https://doi.org/10.1155/2021/5518927.

[58] C. Yang, Z.J. Huang, B.B. Jiang, M.L. Zhu, A.R. Luo, J.F. He, Improved clonal selection algorithm based on the directional update strategy, J. Supercomput. 79 (17) (2023) 19312–19331, https://doi.org/10.1007/s11227-023-05405-x.

[59] B.H. Ulutas, S. Kulturel-Konak, A review of clonal selection algorithm and its applications, Artif. Intell. Rev. 36 (2) (2011) 117–138, https://doi.org/10.1007/s10462-011-9206-1.

[60] C. Yang, B.Q. Chen, L. Jia, H.Y. Wen, Improved clonal selection algorithm based on biological forgetting mechanism, Complexity 2020 (2020), https://doi.org/10.1155/2020/2807056.

[61] T.M. Cabreira, L.B. Brisolara, R.F. Paulo, Survey on coverage path planning with unmanned aerial vehicles, Drones-Basel 3 (1) (2019), https://doi.org/10.3390/drones3010004.

[62] DJ-Innovations, Mavic 3- technical parameters. https://www.dji.com/cn/support/product/mavic-3, 2024.

[63] M. Omoya, I. Ero, M.Z. Esteghamati, H.V. Burton, S. Brandenberg, H. Sun, Z.X. Yi, H. Kang, C.C. Nweke, A relational database to support post-earthquake building damage and recovery assessment, Earthq. Spectra 38 (2) (2022) 1549–1569, https://doi.org/10.1177/87552930211061167.